Microstructure and wear performance of alumina/graphene coating on textured Al$_2$O$_3$/TiC substrate composites

Changxia Liu [a, b*] Junlong Sun [a, b*] Federico Venturi [b] Acacio Rincon Romero [b] Tanvir Hussain [b**]

[a] School of Transportation, Ludong University, Yantai 264025, Shandong Province, China

[b] Faculty of Engineering, University of Nottingham, NG7 2RD，United Kingdom

Abstract: The incorporation of graphene-based nanodispersoids in ceramic coatings is known to enhance the wear behavior of these materials. In this study, for the first time, alumina/graphene nanoplatelets (GNPs) coatings were deposited through Suspension High Velocity Oxy-Fuel (SHVOF) thermal spray on Al$_2$O$_3$/TiC substrate composites, which were laser microtextured with grid and line surface patterns. Dense coatings with around 8-10 µm thickness were obtained by spraying alumina suspension containing 1 wt. % GNPs. The tribological performance of the alumina/GNPs coatings on the Al$_2$O$_3$/TiC substrate composites was evaluated using ball-on-disc sliding wear tests. The alumina/GNPs coated Al$_2$O$_3$/TiC substrate composites textured with grid pattern showed the best tribological performance reaching a steady coefficient of friction (CoF) at lower sliding distances and presenting the lowest wear rate of the Al$_2$O$_3$/TiC substrate composites and the counterbody.

Keywords: SHVOF; Graphene nanoplatelets; Al$_2$O$_3$/TiC substrate composites; Wear performance; Micro texture

1 Introduction

Al$_2$O$_3$/TiC composites proved to be excellent materials for friction and wear applications due to their intrinsic advantages such as high hardness, good chemical inertness, high wear resistance and, low friction coefficient [1]. An effective way to improve the tribological performance of Al$_2$O$_3$/TiC composites relies on the modification of their flat surface. The combined effects of surface texturing and the application of a ceramic coating on the surface are common strategies that help to reduce the contact area and the coefficient of friction, improving the tribological performance of Al$_2$O$_3$/TiC composites.

Surface texturing is an effective and novel technique to improve the tribological performance of mechanical components that creates local grooves to interrupt the flat and smooth areas on the surfaces subjected to mechanical contact [2, 3]. It has been demonstrated that grooves can trap wear debris [4], store

lubricant [5] and also contribute to increasing the load carrying capacity of the sliding surface [6, 7]. In the past decades, the surface texturing has been used in many fields to improve the tribological performances of interfaces, including bearings [8], engine cylinder liners [2, 3], seal rings [9, 10] and cutting tools [11-16].

Enomoto et al. (2010-2012) [11-13] have found that nano-/micro-textured surfaces parallel to the main cutting edge and diamond-like carbon (DLC) coating can effectively improve the lubrication performance at the tool-chip interface and anti-chip adhesion performance of the tool. Similar findings were described by Obikawa et al. (2011) [14] by coating cemented carbide micro-textured tools with TiN and DLC using magnetron sputtering plasma and chemical vapor deposition (PCVD), respectively. Right angle cutting experimental results on A6061 aluminium alloys shows that the friction coefficient and frictional force are lower when tools with micro-grooves parallel to the main cutting edge are used, and the cutting performance is improved by reducing the width or increasing the depth of the texture unit. Jianxin et al. (2013) [15] developed cutting tools with dual functions of soft coating and micro-texture. Results show that the tool-chip friction coefficient, cutting force and cutting temperature of soft-coated and micro-textured cutting tools are significantly lower than those of traditional non-coated micro-textured cutting tools. Kedong Zhang et al. (2017) [16] developed three kinds cutting tools, i.e. cemented carbide cutting tools (WC + 6 wt.% Co) only deposited with TiAlN, cemented carbide cutting tools coated with TAilN+WS_2, and the third is, firstly fabricating nanotexture on TiAlN coatings and then coating WS_2 on the nanotexture. Dry cutting of the quenched steel showed that the shear strength of WS_2 was less than that of TiAlN, which increased the contact lubrication between the tools and the chips. The tools coated with WS_2 film showed excellent dry cutting performance. Rong Meng et al. (2018) [17] studied the cooperative effect of micro texture and W-S-C coating on cemented carbide substrates. Results showed that the tribological behaviors were significantly improved, and laser surface micro-texturing could improve the coating-substrate adhesion strength effectively. Xuemu Li et al. (2019) [18] investigated the combination of WS_2 films and surface textures for improving the friction and wear properties of sol-gel ZrO_2 coatings. Results revealed that the textured samples with the texture coverage of 0.679 showed the lowest friction coefficient and lowest steel ball wear rate, and laser surface micro-texturing could contribute to prolonging the WS_2 films wear life and magnify its lubricating effect.

The incorporation of graphene nanoplatelets (GNPs) into ceramic matrix composites proved to increase the flexural strength and fracture toughness of these materials as they modify the interfacial contact

between the different phases [19-24]. Due to its two-dimensional character, graphene also presents a great potential to improve the tribological behavior of carbon-based reinforced ceramics by decreasing the coefficient of friction (CoF) due to the formation of a thin GNP-rich lubricating tribofilm, formed by the exfoliation of graphene layers from GNPs embedded in the ceramic matrix [25-31]. ZengbinYin, et al. (2018) [26] fabricated TiB_2/TiC ceramic tool material with the addition of Ni and graphene nanoplatelets by spark plasma sintering. Results showed that crack bridging was the most effective toughening mechanism due to the anchoring effect of graphene. Yehong Cheng, et al. (2018) [28] prepared ZrC–SiC–Graphene composite using spark plasma sintering. The multiple length-scale toughening mechanisms of ZrC–SiC–Graphene composite include the macroscopic toughening mechanism of crack deflection and bifurcation and the micro toughening mechanism of graphene bridging, ceramic micro zone tearing, graphene pull-out, graphene and ceramic brick slipping. Xuchao Wang, et al. (2019) [29] investigated graphene reinforced Al_2O_3-based ceramic tool materials and found that graphene avoid excessive grain growth and the weak bonding interface between the ceramic and the graphene induce a pull-out mechanism improving the fracture toughness of the composite. Jingbao Zhang, et al. [31] discussed the tribological performance between 45 hardened steel and Si_3N_4/TiC based composite ceramic tool materials containing 5 wt% graphene platelets. The improvement of the tribological performance could be attributed to the uniform distribution of the adhered tribofilm and the combined effect of graphene pull-out and the contact area between graphene and the friction surface.

Although some recent investigations report the enhancement of the tribological properties of mechanical components used for friction and wear applications thanks to the combination of surface texturing and coating, to our knowledge, this is the first time that GNPs reinforced ceramics coatings were obtained in Al_2O_3/TiC substrate composites using a Suspension High Velocity Oxy Fuel (SHVOF) thermal spray technique. In another word, a lubricating phase (GNPs) and a hard coating (alumina) together to improve the performance of Al_2O_3/TiC substrate composites with micro texture, has not been thought through yet. Thus, the aim of this work is to produce alumina/GNPs reinforced ceramic coatings and study the tribological behavior of textured Al_2O_3/TiC substrate composites with different groove patterns to evaluate the influence of the coating and texturing pattern in the composite wear performance.

2 Experimental procedure

2.1 Substrate material

Hot-pressed Al_2O_3/TiC substrate composites (Zibo Dongtai Co. Ltd., China) of $12\times12\times5$ mm^3 were used as substrate material. Their composition, physical and mechanical properties are reported in Table 1.

Table 1 - Nominal composition, physical and mechanical properties of the Al_2O_3/TiC substrate composites (provided by Zibo Dongtai Co. Ltd., China)

Composition (wt. %)	Flexural strength (MPa)	Hardness (GPa)	Fracture toughness (MPa·m$^{1/2}$)	Density (g·cm^{-3})
Al_2O_3+55%TiC	900±25	23.5±1.3	5.04±0.6	4.76±0.65

Before surface texturing, the surfaces of Al_2O_3/TiC substrate composites were ground and polished to a roughness, $R_a < 0.1$ µm, and then the samples were cleaned with methanol in an ultrasonic bath for 20 min.

The Al_2O_3/TiC substrate composites were textured by a laser ablation method using a commercial XCGX-20 Nd: YAG laser (Jinan Xinchu Co. Ltd., China) with laser power of 14W, a wavelength of 1064 nm and pulse duration of 10 ns. The samples were fixed on an XYZ motion platform with the top surface perpendicular to the laser beam. The microgrooves were engraved on the polished top surface under atmospheric conditions, setting a voltage of 14 V, scanning speed of 20 mm/s, frequency of 20 kHz and through 3 subsequent scans.

The surface texturing was conducted in a square area of 10×10 mm^2. Two surface microtexture patterns were designed: a line pattern, orienting the ablation only in the longitudinal direction, and a grid pattern, obtained after the ablation in the longitudinal and the transverse directions. The patterns consisted of arrayed micro grooves with an interval of 200 µm and a width of 50 µm. The SEM photographs of the micro textures on the top surfaces of the Al_2O_3/TiC substrate composites are shown in Fig. 1.
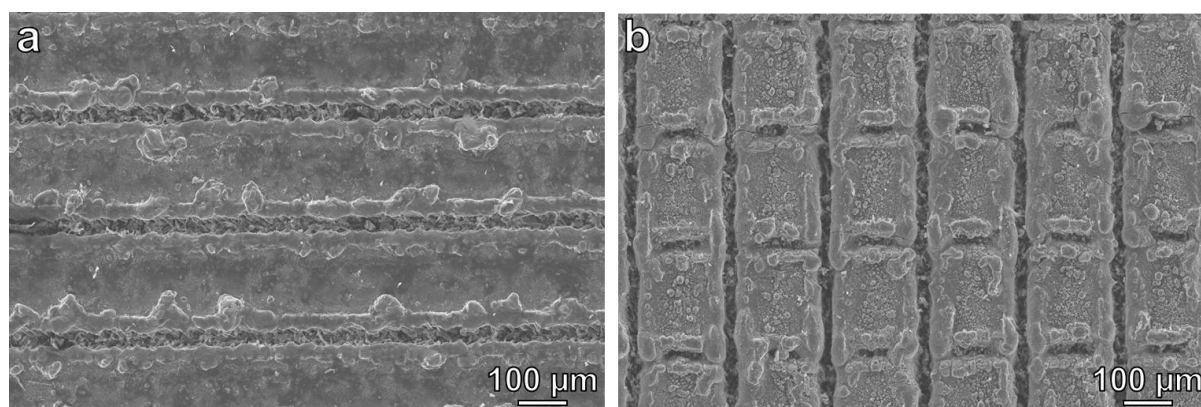

Fig. 1 SEM photographs of the textures on the top surfaces of the Al_2O_3/TiC substrate composites (a) Line. (b) Grid

2.2 Feedstock and coating

Commercial GNPs (abcr GmbH, Germany, Product no. AB 304022) with a nominal thickness of 6–8 nm and an average lateral size of 5 μm were dispersed in a commercially available alumina aqueous suspension (GTV Verschleißschutz GmbH, Germany), characterized by a solid content of ~14 wt. % and nominal average particle size of ~105 nm D50. A 1 wt. % GNP suspension was made in deionized water, including 0.01 wt% sodium dodecyl sulphate surfactant to hinder particle agglomeration. The suspension was ultrasonicated for 30 min using a sonic dismembrator (Fisher Scientific, United Kingdom). The GNPs and the alumina suspensions were merged to a final GNP content of 1 wt. % referred to dry alumina powders, and then the mixture was diluted to a final solid content of 11.78 wt. %, with deionized water. The mixture was kept under mechanical stirring for 60 min before spraying to ensure the dispersion of the GNPs in the alumina suspension. No additional dispersant was required as the commercial alumina suspension already possesses organic additives that help the stabilization. The commercial alumina suspension were dried in a furnace at 150 °C for 3 h to obtain dried powder to conduct further characterization. SEM images of alumina powders dried from the suspension and the as received GNPs powders are shown in Fig. 2.
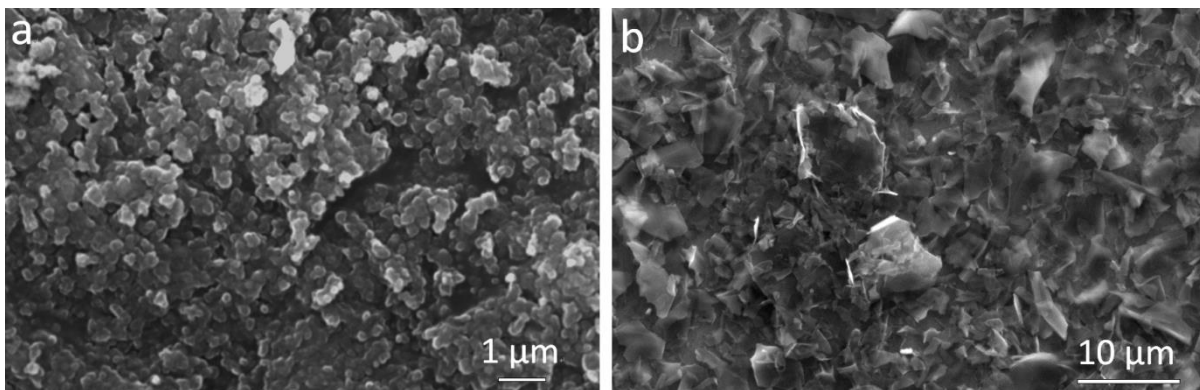

Fig. 2 Secondary electron (SE) scanning electron micrographs of (a) alumina powders dried from the suspension; (b) GNPs powders

The XRD diffractogram of the alumina/GNP feedstock is represented in Fig. 3 where δ-Al_2O_3 (tetragonal) and θ-Al_2O_3 (monoclinic) phases from the alumina suspension and the graphite due to GNPs aggregation during drying are detected.

Alumina/GNPs suspension was sprayed onto the top surface of the textured Al_2O_3/TiC substrate composites, which were previously cleaned with acetone by an ultrasonic bath for 10 min. A TopGun SHVOF thermal spray system (GTV Verschleißschutz GmbH, Germany), modified with a 0.3 mm diameter suspension injector was used, injecting the suspension axially into a 22 mm long combustion chamber. A

schematic drawing of the SHVOF system is shown in Fig. 4, and the spraying parameters used in the study are listed in Table 2 [27].
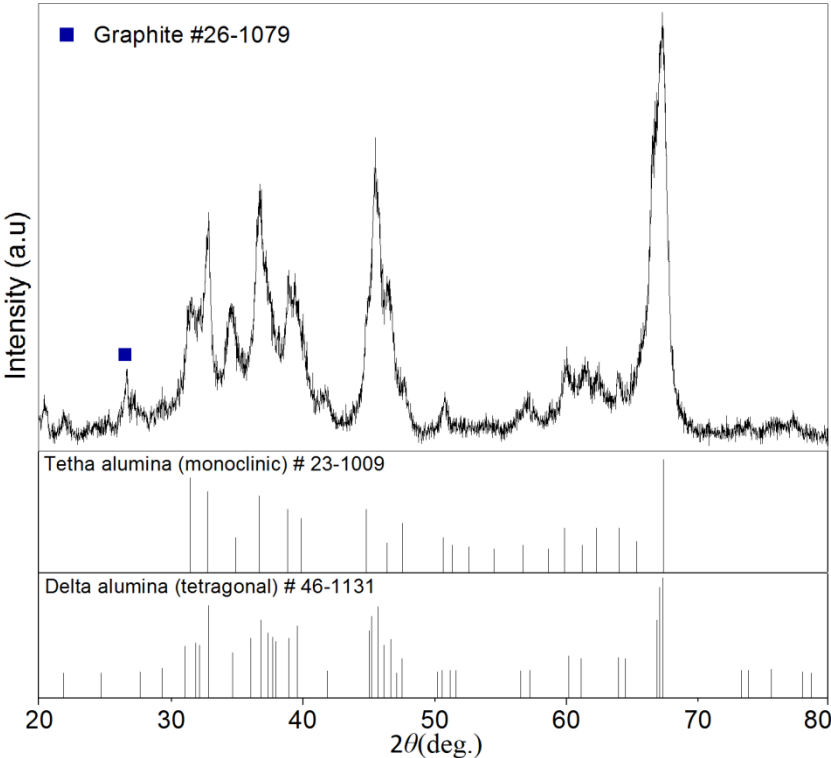

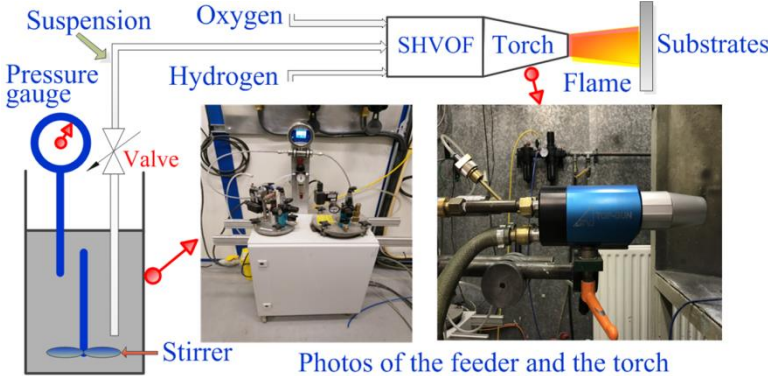Fig. 3 XRD pattern of the alumina+1 wt.% GNPs powders dried from the suspension

Fig. 4 Schematic drawing of the SHVOF system

Hydrogen fuel was combusted in a 22 mm long chamber with 135 mm long, 8 mm wide expansion nozzle. The suspension was fed using a pressurised vessel equipped with a mechanical stirrer and a flowmeter (Bronkhorst, United Kingdom). Before spraying, the substrates were fixed using a holder, mounted onto a carousel rotating around its vertical axis. During and after the spray run, compressed air cooling was applied to the Al_2O_3/TiC substrate composites to prevent overheating.

Table 2 - Spraying parameters for SHVOF of the alumina/GNPs suspension

SHVOF parameters	Value
Feed rate (ml/min)	50
O_2 flow rate (l/min)	307
H_2 flow rate (l/min)	614
Substrate rotation (rpm)	73
Gun vertical velocity (mm/s)	5
Substrate linear velocity (m/s)	1
Pass spacing (mm)	4.1
Number of gun passes	2
Gun stand-off distance (mm)	85

Alumina/GNPs suspension was also sprayed onto the top surface of the non-textured Al_2O_3/TiC substrate composites, however, the expected coated samples with good bond strength between the coating and the substrate in the non-patterned case could not be obtained, due to the low surface roughness of the substrate (less than 0.1 μm), and also sand blasting did not have any effect to increase the substrate surface roughness for the Al_2O_3/TiC substrate composites are too hard and too brittle. It indicates laser texture is a means to allow coating deposition on an otherwise "intractable" surface.

2.3. Vickers microhardness and fracture toughness

Microhardness and fracture toughness measurements were performed using the Vickers indentation method. As the Al_2O_3/TiC substrate composites were too hard to be cut and prepare a cross section samples, the measures were carried out in Alumina/GNPs coatings with a thickness of ~30 μm that were sprayed on stainless steel substrates using the same spray parameters as the coatings sprayed on Al_2O_3/TiC substrate composites but increasing the number of gun passes to 6. The indentations were made evenly distributed and at regular intervals on the polished cross sections (R_a = 0.1 μm) using a Buehler 1600 Series Microhardness Tester (Buehler, USA) equipped with a standard diamond pyramid indenter. The applied load was 50 gf for 5 s, under which conditions the indentation size was sufficiently large to be measured accurately, without crack formation. A load of 200 gf was used in order to yield cracks at the indentation tips to measure the fracture toughness. For hardness and fracture toughness, the average value of ten indentations is reported to minimize the relative error. The following equation developed by Evans and Charles [32] was used to calculate fracture toughness:

$K_{IC}=0.16 \cdot (c/a)^{-1.5} \cdot H \cdot a^{0.5}; c/a \geq 2.5$ (1)

where K_{IC} was the fracture toughness (MPa·m$^{1/2}$), c is the average crack length from the indents' tips (μm),

a is the half average length of the indent's diagonal (μm), and H was the Vickers microhardness measured

from the indent (GPa).

2.4. Wear behavior

Ball-on-flat dry sliding wear tests were carried out using a ball-on-flat tribometer (Ducom Instruments,

The Netherlands). A 6 mm diameter alumina ball (Dejay Ltd, United Kingdom) was used as a counterbody,

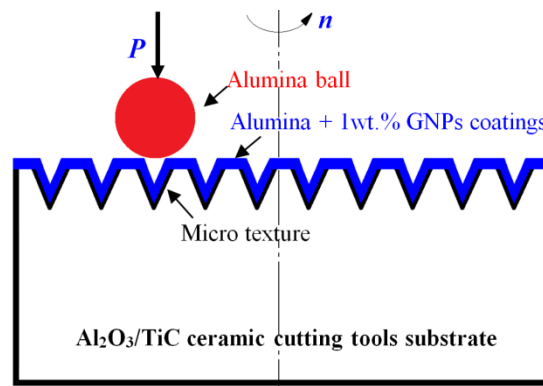a schematic diagram of the friction and wear test is shown in Fig. 5.

Fig. 5 Schematic diagram of the friction and wear tests

Before the wear tests, both the counterbody and the coated samples were cleaned in an ultrasonic bath

(5 min in acetone plus 5 min in ethanol) and dried in air. The tests were carried out in ambient conditions

(40–60% relative humidity, room temperature) for 30 min at a linear sliding speed of 20 mm/s using a load

of 10 N and the friction coefficient, μ, was continuously registered during the tests. One test was conducted

for each sample. The specific wear rate was calculated via the following equation:

$W=V/(L \times F)$ (2)

where W is the specific wear rate (mm^3/Nm), L is the sliding distance (m), F the force applied (N) and V the

volume of material removed (mm^3). For both coated and uncoated Al$_2$O$_3$/TiC substrate composites, the

volumetric material loss, V, could be calculated by multiplying the wear track length (circumference of the

alumina ball movement circle) and the effective area of material loss, which was obtained by measuring

eight cross-sectional profiles at different locations along the wear track length, with an Infinite Focus

Advanced 3D System (Bruker Alicona, Austria). Each of the eight profiles was obtained by a summation

over 20 adjacent cross sectional profiles and averaged. The wear rate of the alumina ball was also

calculated from the worn scar on the ball. This could be considered as a spherical crown [33], whose wear volume could be calculated based on integral operation [34]:

$$V = \int_{\frac{\sqrt{D^2-d^2}}{2}}^{D/2} \pi(\frac{D^2}{4} - y^2)dy = \frac{1}{12}\pi D^3 - \frac{1}{24}\sqrt{D^2 - d^2}(2\pi D^2 + \pi d^2) \qquad (3)$$

where D is the diameter of the alumina ball and d is the diameter of the worn scar.

2.5. Characterization

The surface roughness of the microtexture before spraying was measured using the Infinite Focus Advanced 3D System. The topographies of the powders, the textured surface samples and the wear tracks were observed by scanning electron microscopy (SEM) (JEOL 6490, Tokyo, Japan), using secondary electron (SE) mode. The elemental compositions of the samples were obtained by Energy Dispersive X-Rays Spectroscopy (EDX) (INCA 350, Oxford Instruments, United Kingdom). The phase compositions of the dried alumina/GNP feedstock suspension and the Al_2O_3/TiC substrate composites before and after coating were determined using X-ray diffraction (XRD) analysis by means of a Bruker D8 advance diffractometer equipped with Da Vinci X-ray detector (Bruker, Germany), in Bragg-Brentano θ-2θ geometry using Cu K_α radiation (1.5406 Å) produced at 20 kV and 5 mA. The diffractograms were scanned from 20° to 90° 2θ, setting a step size of 0.02° and time per step of 0.1 s. The coatings were also analyzed using the same diffractometer and setting a glancing angle configuration fixing the x-ray beam at 2°, using 40 kV–40 mA, $2\theta = 20$–68°, a step size of 0.01° and a time per step of 0.2 s. The phase identification of the XRD results was completed using EVA 5.1 program package, supported by ICDD data from the PDF-2 database. Raman spectroscopy was performed to detect the survival of GNPs after coating, as well as that of GNPs on the wear track after wear testing for coated ones using a LabRAM HR spectrometer (Horiba Jobin Yvon, Japan) equipped with an automated XYZ stage (Märzhäuser). For the Raman spectroscopy of GNPs after coating, a green laser with a wavelength of 515 nm was used, as to that of GNPs on the wear track after wear testing for coated ones, the laser type was He-Ne with a wavelength of 532 nm and a maximum laser power of 130 mW. The possible Ti oxide compounds on the wear track of uncoated sample were determined using an inVia Micro-Roman confocal spectroscopy system (Renishaw, Wotton-under-Edge, Gloucestershire, UK) with a laser wavelength of 532 nm and a maximum power of 2.25 W.

3 Result and discussion

3.1. XRD characterization

XRD patterns of the Al$_2$O$_3$/TiC substrate composites as-provided without texture, after texturing and after texturing and coating are shown in Fig. 6 (a).

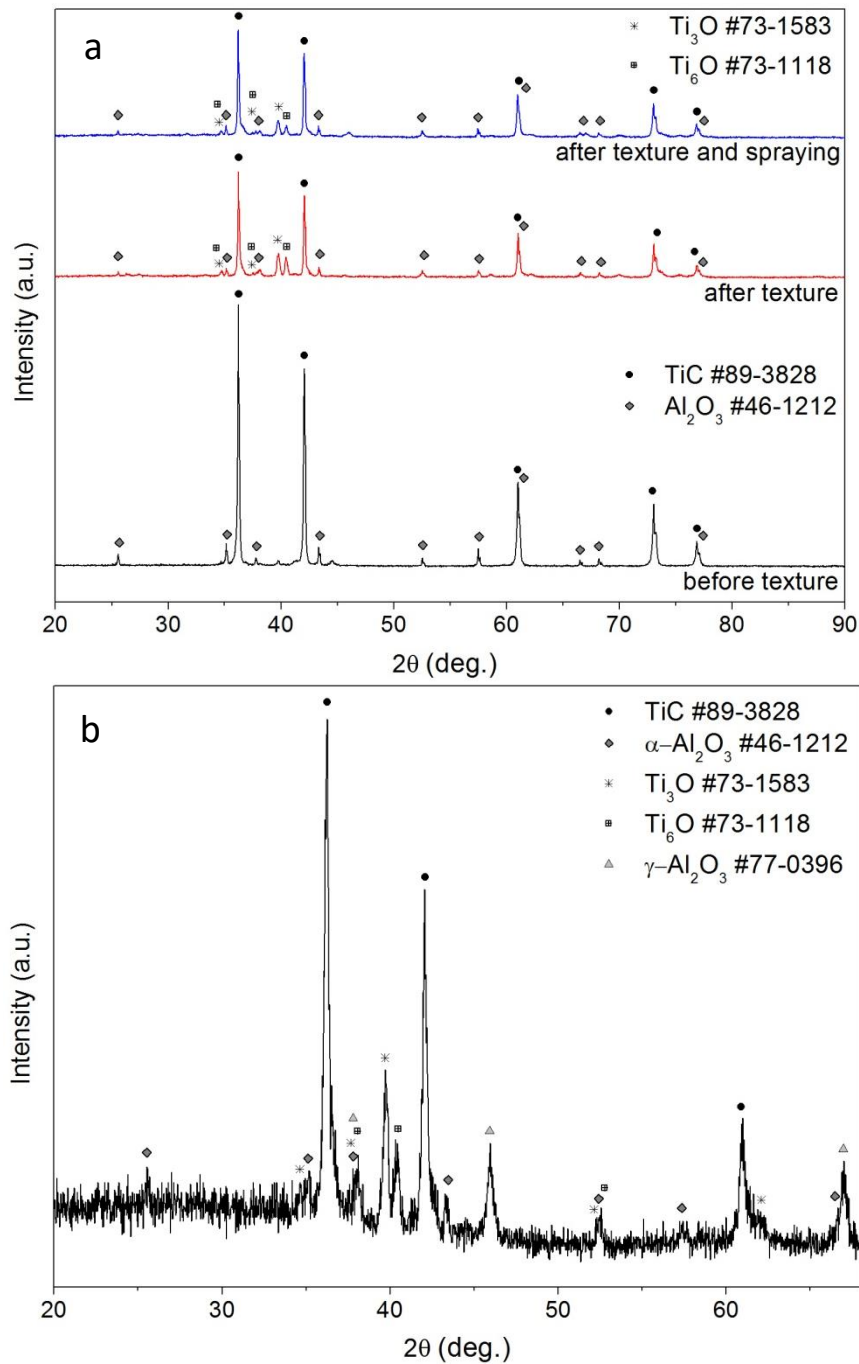Fig. 6 XRD patterns of the Al$_2$O$_3$/TiC substrate composites without texture, with texture before and after spraying (a) and coated sample with a glancing angle (b), with no evidence of GNPs after spraying, due to low constituent weight %

Only Al_2O_3 and TiC phases were detected in the samples before the laser texturing process which was in agreement with the compositions reported in Table 1. After the laser texturing process small proportions of Ti_3O and Ti_6O were also detected, these phases were also present in the samples after texture and after the spraying process as the coatings were thin. Ti_3O and Ti_6O phases, were classified as oxygen-deficient nonstoichiometric oxides, they were formed during the micro texturing process revealing that some oxidation of the substrate happened during the interaction of the laser ablation process in air. The presence of Ti_3O and Ti_6O after texturing the samples might be due to oxygen ordering in Ti, which could be explained by oxygen diffusion in Ti lattice. Some researchers [35-38] have shown that the higher accumulated laser fluency, the higher degree of oxidation, i.e., with high oxygen diffusion, the more the samples will trap oxygen in the melted phase. It has also been reported that TiC could be easily oxidized forming TiO_2 at high temperatures [39-46]. However, no peaks of TiO_2 were found, indicating that the complete oxidation of TiC during laser ablation might take place in an environment with sufficient oxygen supply.

No obvious phase changes between the patterns of the Al_2O_3/TiC substrate composites before and after spraying are detected, as the coating is too thin it cannot be detected in Bragg-Brentano geometry due the high level of x-ray penetration in the sample, for this reason the coated samples were studied with glancing angle configuration. The diffractogram is shown in Fig. 6 (b) where Al_2O_3, TiC, Ti_3O and Ti_6O phases described before in the samples before and after spray are present. However, also it can be noticed the presence of the γ-Al_2O_3 phase. This γ-Al_2O_3 phase arises from the transformation of the initial feedstock, which consists of δ-Al_2O_3 (tetragonal) and θ-Al_2O_3 (monoclinic), during the spray process. The initial alumina melts and suffers a rapid solidification leading to the formation of γ-Al_2O_3 which is consistent with the findings of Murray et al. [27] and Owoseni et al. [47] concerning the phase transformation of alumina phases using SHVOF. The lack of peaks for GNPs was mainly due to the fact that the amount of GNPs was too small to be detected by XRD [48].

3.2. Coating thickness, Vickers microhardness and fracture toughness

It was not possible to obtain a cross-section sample to measure the thickness of the coatings on the micro texture surface as the substrate was too hard to be cut with traditional metallographic sample preparation methods. Al_2O_3/TiC substrate composites without texture were also coated using the same spraying parameters, to evaluate the coating thickness measuring it at the edge face of the substrate with a flat surface. The thickness of the alumina/GNPs coatings evaluated in this way was between 8-10 µm. The

Vickers microhardness and fracture toughness of such a thin coating was also difficult to quantify. Thus, these mechanical properties were measured in alumina/GNPs coatings obtained in a 316 stainless steel substrate using the same spraying parameters but changing the number of gun passes changed from 2 to 6. Then a cross-section sample with a coating thickness of ~ 30 µm could be obtained to determine the micro Vickers hardness and fracture toughness of the coatings. The hardness and fracture toughness of the alumina/GNPs coatings were (9.5 ± 2.0) GPa and (2.0 ± 0.7) MPa·m$^{1/2}$, respectively.

3.3. Top surface microstructural analysis

A quantitative characterization of the 2D surface morphology of the Al_2O_3/TiC substrate composites before coating is shown in Fig. 7, it was carried out in order to evaluate the particular surface morphology before coating.
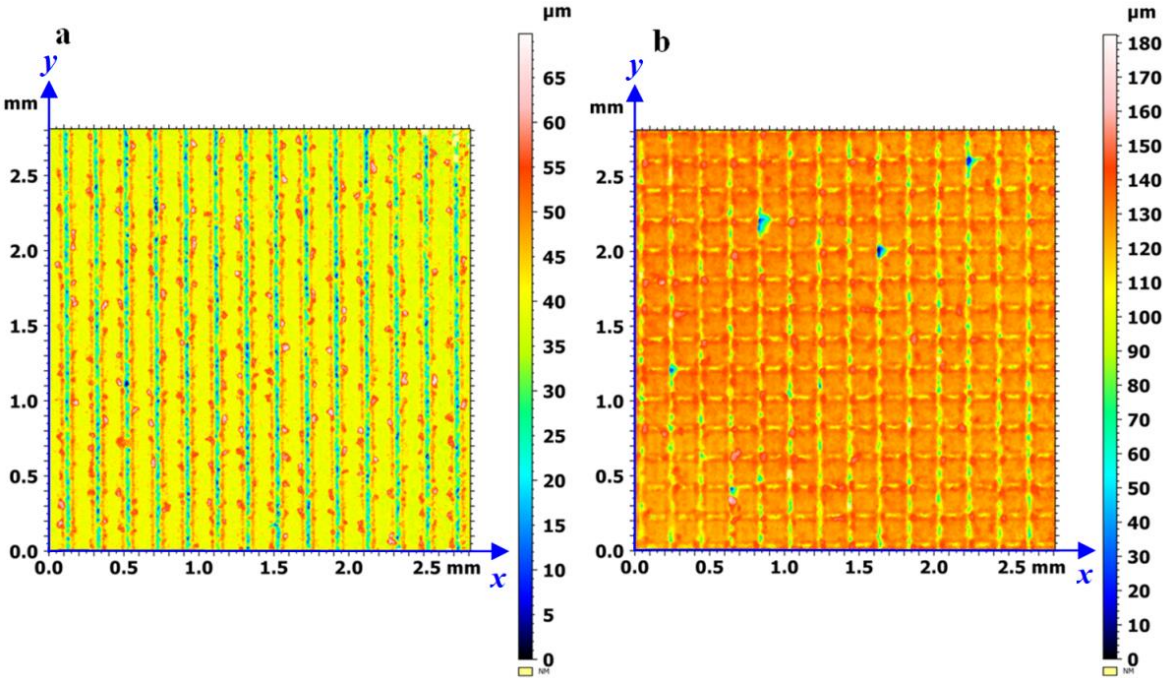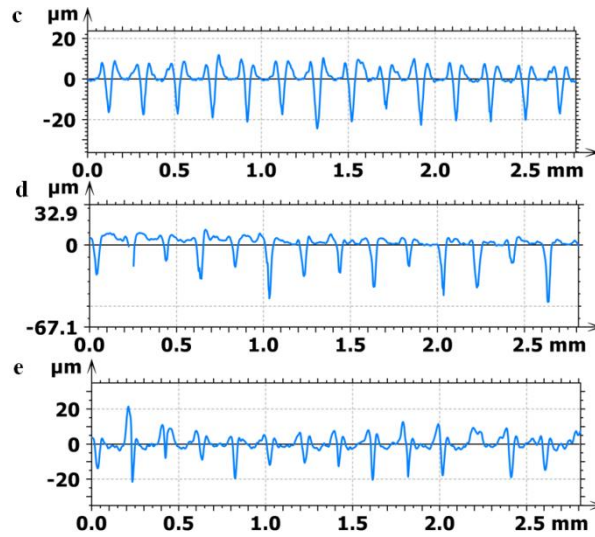
Fig. 7 Quantitative characterization of the surface morphology (2D) of the Al_2O_3/TiC substrate composites before coating (a) Line. (b) Grid. (c) Profile curve along *x* for line texture. (d) Profile curve along *x* for grid texture. (e) Profile curve along *y* for grid texture

Evenly distributed grooves in a line and a grid texture pattern could be observed in Fig. 7 (a) and (b) respectively, which was in agreement with the SEM analysis (Fig. 1). The cross-sectional height profile images of the line pattern along x direction and grid texture along x and y direction are shown in Fig. 7 (c), (d) and (e), respectively. It can be seen from the profiles in Fig. 7 that Al_2O_3/TiC substrate composites surfaces had evenly distributed grooves, whose width, depth and period were around 50 μm, 20 μm and 200 μm, respectively. As can be observed in Fig.7, a series of small peaks is present next to the grooves. This is an unavoidable byproduct of the laser ablation process as part of the material removed accumulates at the sides of the groove, and this is particularly evident for shallow grooves and short pitch. This can play a role in modifying surface roughness, however, from Fig.8 it can be seen how these features have been smoothed by the coating process, leaving intact the initial deep grooves.

As could be seen from Fig. 8 (a) and (c), the initial shape and structural characteristics of the line and grid microtextures remain unchanged after the coating process.
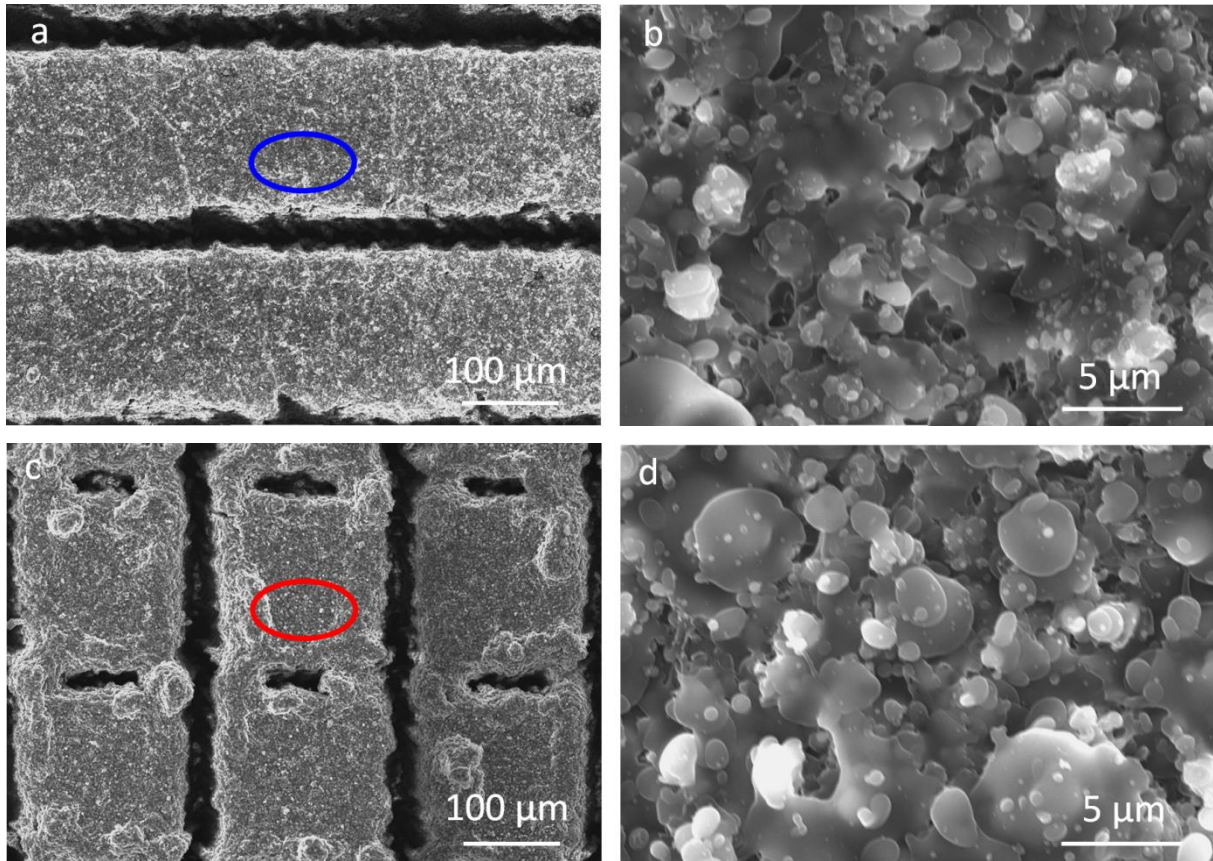
Fig. 8 SEM images showing the surface morphology of the coatings (a) Whole view of the coatings on the line texture. (b) Enlarged area marked with a blue ellipse. (c) Whole view of the coatings on the grid texture. (d) Enlarged area marked with a red ellipse

The alumina/GNPs coatings present a good coverage of the microtextured surfaces, which preserves the line and grid morphological features if compared to Fig. 1. High magnification SEM images of the coatings with line and grid texture are shown in Fig. 8 (b) and (d), respectively. The splats which constitute the building blocks of the coating appear larger and having smoother edges in Fig. 8 (b) and (d) if compared to alumina powder in Fig. 2 (a). This is due to the melting or partial melting, and deformation upon impact in forming pancake-shaped splats. The more the deformation, the stronger the bonding with the substrate and between coating particles, which is beneficial to the formation of a more compact coating with low porosity. Nevertheless, not all the particles reach the substrate in a molten state due to fast solidification, and solidified particles generate more porous coatings. In fact, different particle sizes and different in-flight particle velocities and trajectories led to different solidification times. No evidence of GNPs was found in the SEM images of the top surface of the coatings either for the line or grid texture samples, as they are elusive due to their low concentration and low density and thickness.

In order to confirm the survival of GNPs in the coatings, Raman spectroscopy was performed on the surfaces of the alumina/GNPs coatings, as is shown in Fig. 9.
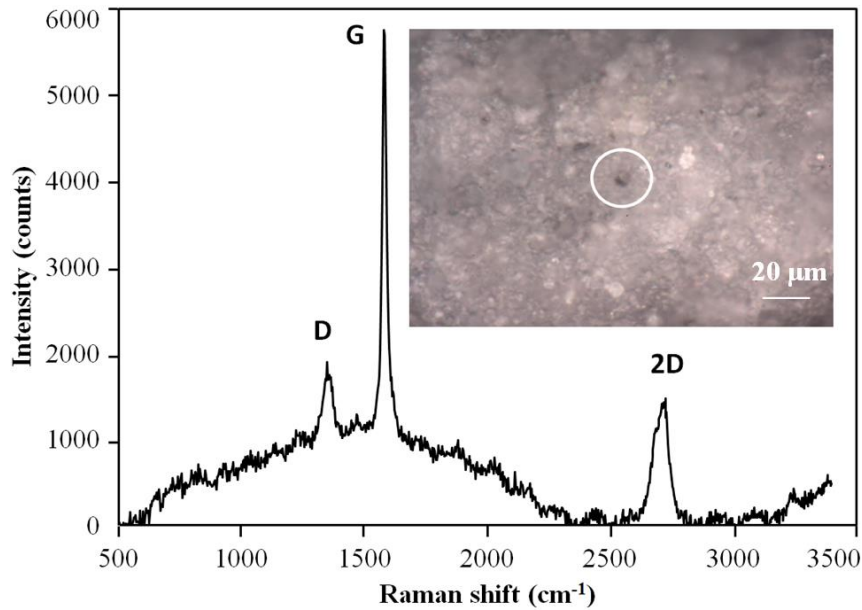

Fig. 9 Raman spectra of the alumina/GNPs coatings on the Al_2O_3/TiC substrate composites with grid texture

GNPs bands are centered at the same Raman shift of those of graphite; in fact, they can also be regarded as a very thin chunk of graphite. Using a laser excitation of 515 nm there are three distinctive bands[27, 49-50]: (1) the G band of free-standing graphene, shown as the most intense band at ~1580 cm^{-1}, which is induced by a high frequency E_{2g} optical phonon in graphene and associated with the presence of well-graphitized structure; (2) the D band with the typical Raman shift of ~1350 cm^{-1}, at which an A_{1g} breathing mode of six-atom rings, correlated with lattice defects, is found, as typical for defective single-layer graphene and nanocrystalline graphite; (3) the 2D band (sometimes referred to in the literature as the G′peak), which appears at ~2700 cm^{-1}, is associated with few-layers graphene structures and yields information on the degree of order between them. A higher ratio between D and G bands intensities indicates a higher amount of intralayer defects (vacancies or substitutional atoms). The penetration of the laser into the sample under the applied experimental conditions was approximate ~ 6 μm [27], this penetration depth is lower than the thickness of the coating, evading the interference of carbonaceous compounds from the substrates in the spectrum.

It could be seen from Fig. 9 that all the D, G and 2D bands are present in the recorded spectra, confirming the presence of GNPs [27]. Furthermore, the bands' relative intensities I_D/I_G = 0.33 and I_{2D}/I_G =

0.28, indicate a small number of intralayer defects and a good interlayer ordering, ensuring GNPs have undergone minimal structural degradation upon SHVOF thermal spray compared to pristine GNP (I_D/I_G= 0.19 ± 0.10; I_{2D}/I_G= 0.25 ± 0.04) [51].

3.4. Wear testing

CoF against the sliding distance at the speed of 20 mm/s under a normal load of 10 N for the textured Al_2O_3/TiC substrate composites before and after coating are shown in Fig. 10.
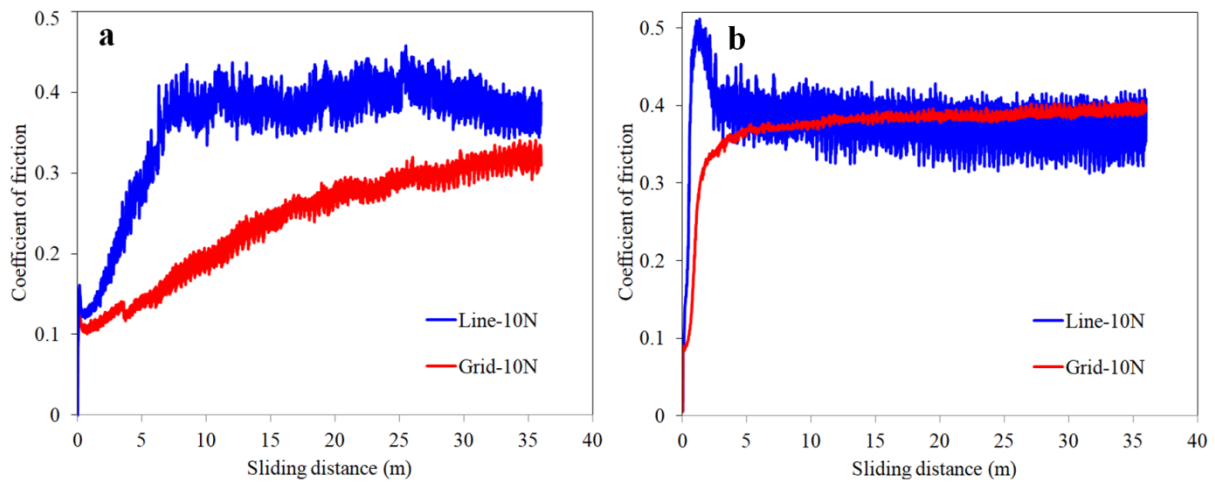

Fig. 10 Coefficients of friction against sliding distance for the Al_2O_3/TiC substrate composites from wear tests (a) before spray. (b) after spray

In general, wear mechanisms present two stages, an initial bedding-in stage and a second stage where the CoF remains steady called stable stage. Both line and grid samples before spray exhibited a long bed-in stage, which lasted around 7 and 30 m, respectively. The behavior is very different after spray, with a bed-in stage of around 3 m and a following stable stage. The alumina/GNP coating showed a lower microhardness and lower fracture toughness compared to that of the substrate, therefore, as expected from a softer coating, the smoothening of the micro-convex bodies at the contacting interface occurs more rapidly and yields quickly to a stable CoF. The Al_2O_3/TiC substrate composites are instead harder and require longer sliding distance for this to occur. With the continuation of the wear test, in the stable stage, some of the micro-convex bodies peeled off, and the contact surfaces were smoothened and polished gradually, leading to the increased contact area and decreased contact stress. The CoF tended to be stable at this stage and only small fluctuations in the CoF due to non-perfect planarity of the sample are detected. In addition, after spray the CoF of line and grid textured samples behave more similarly, possibly due to the coating which smoothens some of the texturing features and dominates the CoF behavior. Conversely, before spray

the texturing pattern plays a major role and a more evident difference between line and grid emerges, with higher CoF in the line case.

The average CoF in steady-state of the Al_2O_3/TiC substrate composites with line and grid texture before coating (Fig. 10 (a)) was around 0.37 and 0.32 respectively. Meanwhile, those of the samples with line and grid texture after coating was slightly higher than that of before coating, both reaching an average value up to around 0.38. This increase in the steady-state CoF of the samples after coating could be explained due to the presence of a higher amount of wear debris, generated by the additional alumina/GNPs coating and changing the two-body wear mechanisms to three-body wear. Moreover, the presence of Ti_3O and Ti_6O phases formed during the laser ablation, as well as some other oxide compounds that probably formed in the debris by the tribo-oxidation of TiC, which will be mentioned in Section 3.5, might play a significant role to decrease the CoF of the samples before coating, since Ti oxides have been proved to be a useful lubricant additive in wear applications [52-56].

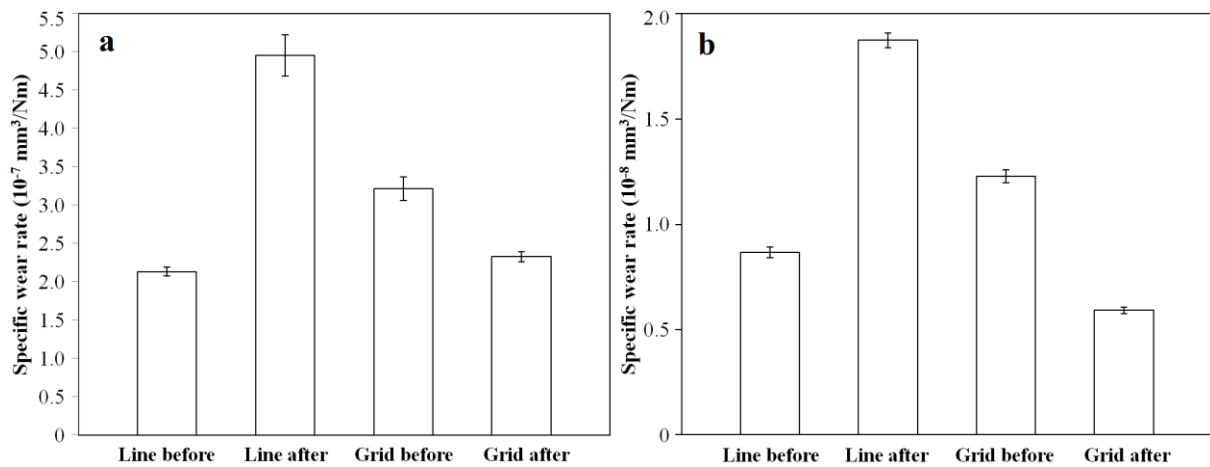Specific wear rates of the Al_2O_3/TiC substrate composites and the counterbodies are shown in Fig. 11.

Fig. 11 Specific wear rates of the four kinds of samples (a) and the sliding balls (b) at a load of 10 N

Comparing the line and grid textures before coating, it emerges how the grid texture yields a higher specific wear rate of both the sample and the counterbody, with an increase around 30% compared to the line texture. Considering the sample, the contacting area is smaller in the grid texture case as a double amount of grooves is present, yielding a higher contact pressure and therefore a higher wear rate. Regarding the counterbody wear, the higher capability of the grid texture in collecting the wear debris in the grooves and directing it outside the contact area yields a more efficient "cutting" of the counterbody.

Considering now the effect of the coating on the two different texture patterns, in the line texture case, it can be seen that the wear rate of the samples presented a higher wear rate with coating $((4.96\pm0.27)\times10^{-7}$ mm^3/Nm) than without the coating $((2.13\pm0.06)\times10^{-7}$ mm^3/Nm). Similarly, the counterbody against the Al_2O_3/TiC substrate composites with line pattern after coating shows the highest wear rate of $\sim1.87\times10^{-8}$ mm^3/Nm. As also reported in Fig. 10, the coated line textured sample shows the highest CoF of all, possibly explaining the higher wear rate. An opposite behavior is detected in the grid texture case, since both the samples and the counter body present lower wear rates with the alumina/GNPs coating (Fig. 11 (b)). Here, the coating reduces the effect of the texturing by smoothening it, therefore the contact pressure is reduced and so is the capability of the grooves to carry away the debris, reducing the specific wear rates of both the sample and the counterbody.

It can be concluded that the alumina/GNPs coatings showed an improvement in the tribological performance on the Al_2O_3/TiC substrate composites with grid texture, whereas the contrary is true for the coated samples with the line texture.

3.5. Raman spectroscopy of the possible Ti oxide compounds and graphene on the wear tracks

In order to detect the presence of the possible Ti oxide compounds on the wear track of uncoated grid textured samples, as well as that of the graphene on the wear track of the coated grid textured samples, Raman spectroscopy on the wear track of the grid textured samples before and after coating was performed, which are shown in Figs.12 and 13.
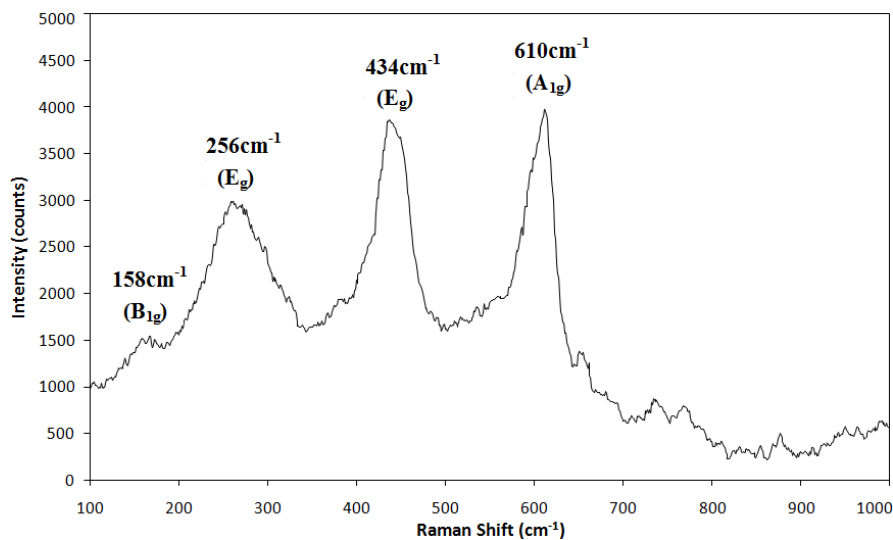

Fig. 12 Raman spectroscopy on the wear track of the grid textured samples before coating
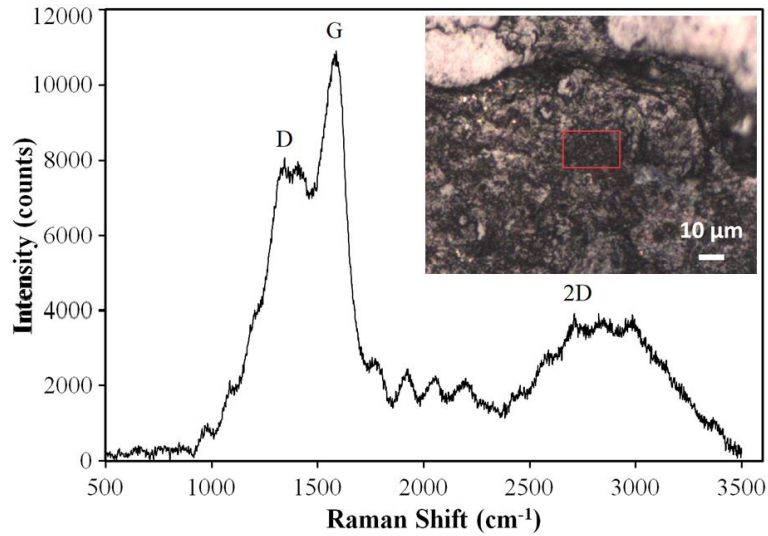
Fig. 13 Raman spectroscopy on the wear track of the grid textured samples after coating

From Fig.12, one could see that the Raman spectroscopy obtained from the wear track of the grid textured samples before coating showed a series of peaks correlated to rutile, 158, 256, 434 and 610 cm^{-1} [57]. B_{1g} represents the Raman vibration caused by the bending vibration mode of O-Ti-O. The peaks at 256 and 434 cm^{-1} (E_g) are the Raman vibration caused by the rocking and twisting vibration modes of O-Ti-O. A_{1g} belongs to the Raman vibration caused by the axial antisymmetric stretching and equatorial bending vibration mode of O-Ti-O. TiO_2 was probably formed in the debris by the tribo-oxidation of TiC, due to possible frictional heating during the dry-sliding condition. This result was in line with that obtained by C. Magnus [58] and Bowen Zheng [59].

From the Fig.13 it could be noticed the characteristic G, D and 2D bands, which had been proved to be the critical spectroscopic feature peaks of graphene and confirmed the presence of GNPs on the wear track [27]. The relative intensities of the different bands is $I_D/I_G = 0.73$ and $I_{2D}/I_G = 0.31$ respectively. The I_D/I_G bands' relative intensity increases compared with the samples before wear test (Fig.9) indicating interlayer structural degradation after the wear test, related with the GNPs amorphisation and partial oxidation as a result of the heat and friction generated by the counterbody [51]. The I_{2D}/I_G intensity ratio is also of similar magnitude before and after the wear test, however the 2D band shows the appearance of the higher order D+D' and 2D' bands at around 2900 cm^{-1} and 3200 cm^{-1} respectively, with a significant broadening and overlapping, indicating also a higher level of interlayer disorder compared to the GNPs after coating.

The presence of rutile TiO_2 and graphene in wear track would beneficially provide easy-shear and low friction properties at the interface, which will be discussed in the following section.

3.6. Worn morphologies of the Al_2O_3/TiC substrate composites

SEM images of the Al_2O_3/TiC substrate composites with line texture before and after coating (load = 10 N, sliding speed = 20 mm/s, time = 30 min) are shown in Figs. 14 and 15, respectively.
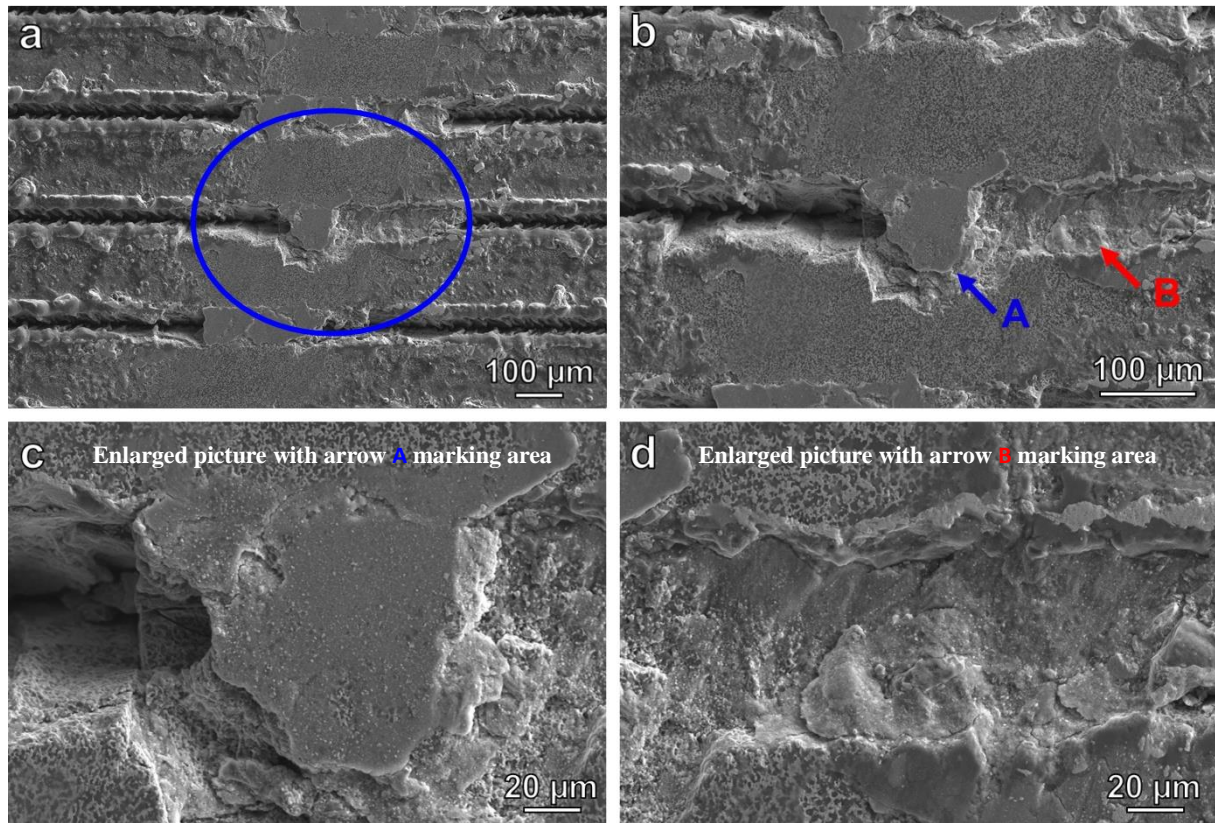

Fig. 14 SEM images of the wear track of the Al_2O_3/TiC substrate composites with line texture before coating (Load=10N, sliding speed=20mm/s, time=30min) (a) Whole view of the wear track. (b) Enlarged area marked with a blue ellipse in the whole view. (c) and (d) Enlarged area marked with A and B in (b)

Some friction films were formed on the wear track of the samples as can be seen in Fig. 14 (a). The EDX analysis of these friction films shows that they are mainly composed of Al, Ti and O, in a 32.7, 22.8 and 44.4 wt. %, respectively. These films might include the oxygen-deficient nonstoichiometric oxides of Ti such as Ti_3O and Ti_6O (detected by XRD analysis), and rutile TiO_2 that might have formed by tribo-oxidation of TiC fragments in the debris (detected by Raman spectroscopy on the wear track of the grid textured samples before coating), that might help to reduce the CoF. In addition, the capability of the grooves to capture the wear debris can be observed, which contributed to keeping the CoF in a relatively low value for the line-textured Al_2O_3/TiC substrate composites samples without coating. Fig. 14 (c) and (d) depicts a brittle failure of the friction films that occurs during the friction process, indicating a major mechanism of fatigue spalling for the wear behavior.

Discontinuous films were found on the wear track of the sample textured with line after coating (Fig. 15 (a) and (b)).
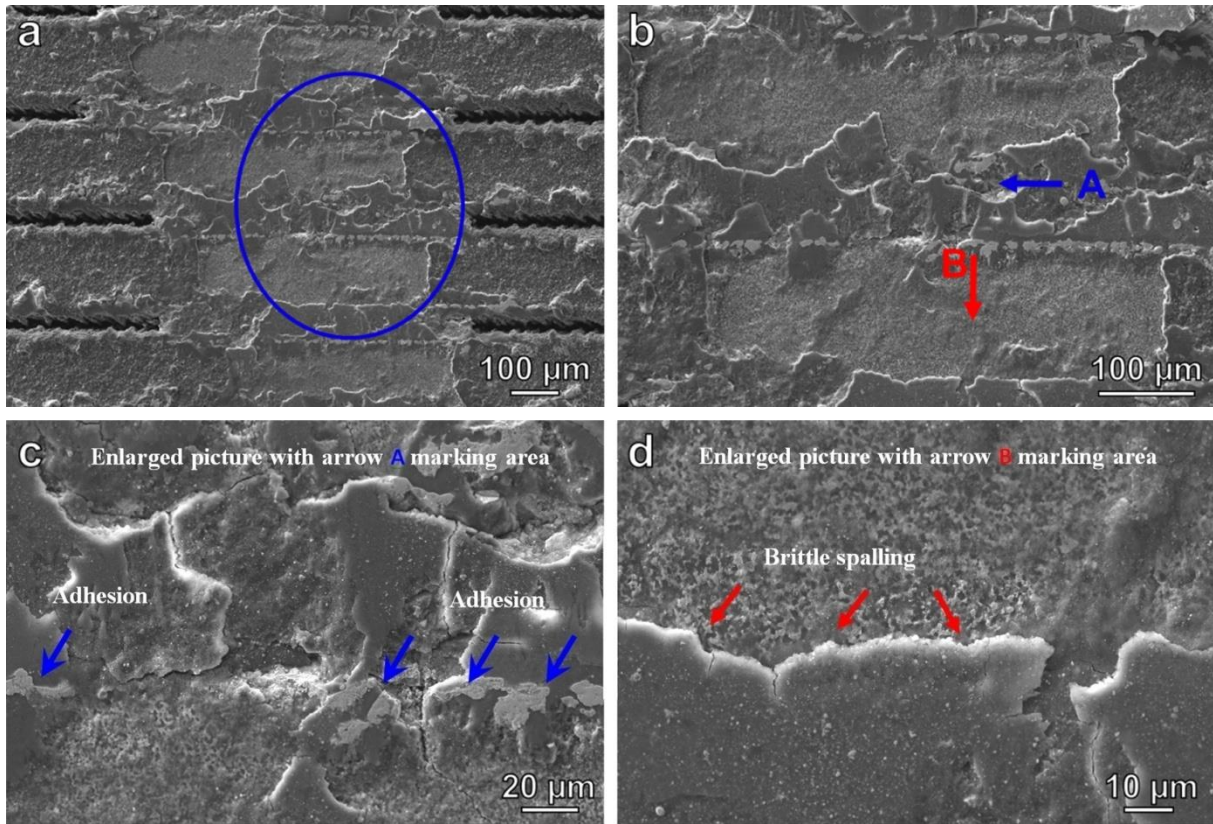

Fig. 15 SEM images of wear track of the Al$_2$O$_3$/TiC substrate composites with line texture after coating (Load=10N, sliding speed=20mm/s, time=30min) (a) Whole view of the wear track. (b) Enlarged area marked with a blue ellipse in the whole view. (c) and (d) Enlarged area marked with A and B in (b)

Here, a higher amount of material filling the grooves is present, compatibly with the measured higher CoF and wear rate, showing a higher amount of cracks and an overall less compact structure. The removal of the coating from the flat area between the grooves can be observed. The close-up view of the wear scar revealed some adhesions (marked with blue arrows in Fig. 15 (c)) and some brittle spalling (Fig. 15 (d)) of the alumina/GNPs coatings. The brittle spalling can be seeded by the small peaks generated by laser texturing at the sides of the grooves. An interesting phenomenon was observed in the samples textured with line pattern as the wear rate of the uncoated sample was much lower than the one presented after coating. This is attributed to the existence of Ti$_3$O and Ti$_6$O phases that were formed on the edge of the grooves during the laser ablation, as well as rutile TiO$_2$ that might have been formed by the tribo-oxidation of TiC fragments in the debris, as they can provide easy-shear and generate a lubricant film during the sliding process to decrease the friction. In the Al$_2$O$_3$/TiC substrate with line texture after coating, the influence of

lacking Ti_3O, Ti_6O or rutile TiO_2 at the wear interface between the coating and the counterbody might be one reason that led to the higher wear rate. Another reason might be related to the obvious delamination of the film (Fig. 15 (a) and (b)), which could cause a sudden loss of several micrometres' worth of thickness from the sample surface, further releasing abrasive alumina debris in the contact area. The main wear mechanisms of alumina/GNPs coatings on the line textured Al_2O_3/TiC substrate were brittle spalling, adhesive and abrasive wear.

SEM images and EDX analysis of the wear track of the Al_2O_3/TiC substrate composites with grid texture before coating are shown in Fig. 16.
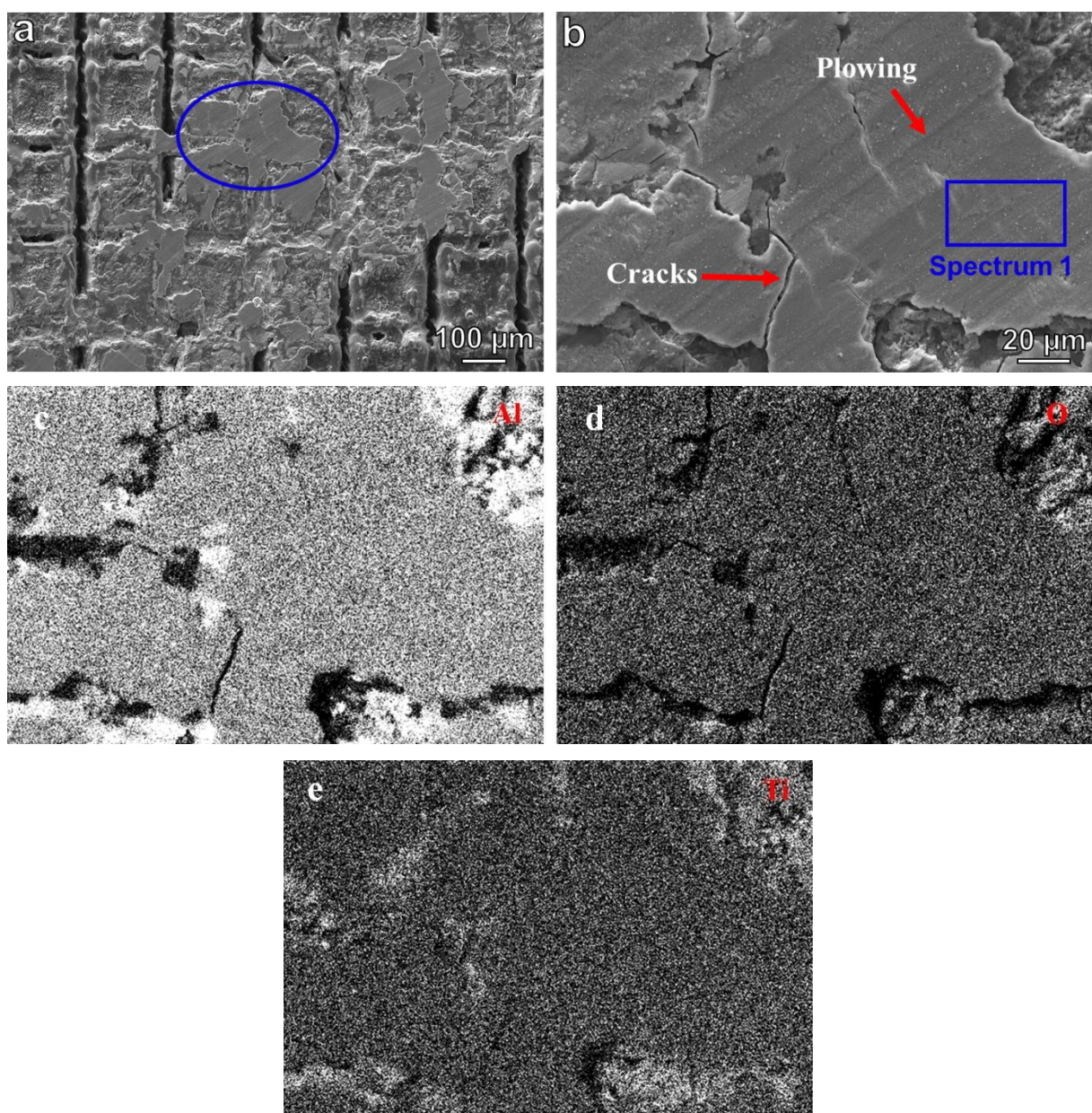

Fig. 16 SEM images and EDS of the wear track of the Al_2O_3/TiC substrate composites with grid texture before coating (Load=10N, sliding speed=20mm/s, time=30min). (a) Whole view of the wear track. (b)

Enlarged area marked with a blue ellipse in the whole view. (c) (d) and (e) Mapping analysis showing Al, O and Ti elements distribution in (b)

Discontinuous friction films can be observed in the marked area in Fig. 16 (a), they are mainly distributed filling the grooves along the wear track, on them some cracks could be detected. From the magnified area presented in Fig. 16 (b), it could be seen that plowing and cracks formed. It was proved that the friction films were composed of Al, O and Ti elements (38.8, 16.0 and 45.2 wt. %, respectively) by the mapping analysis of the whole area presented in Fig. 16 (b), suggesting that the friction films were mainly composed of Al_2O_3 and Ti oxide compounds, e.g. Ti_3O, Ti_6O or rutile TiO_2, which might play a significant role in decreasing the CoF and the wear rate of the samples with grid texture before coating, resulting in a relatively low CoF and wear rate. The main wear mechanism of the Al_2O_3/TiC substrate composites with grid texture before coating was brittle fracture and plowing.

SEM images of the wear track of the samples textured with grid pattern after coating are shown in Fig. 17.
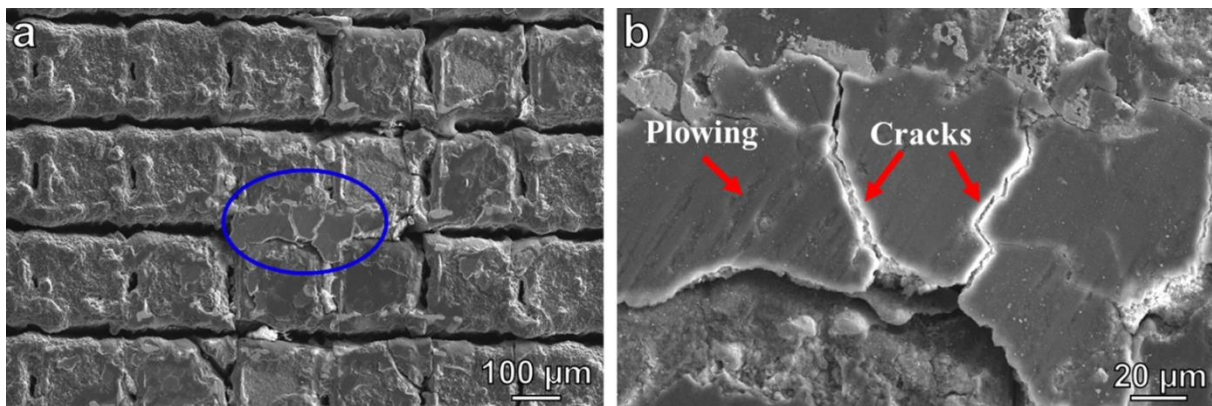

Fig. 17 SEM images of the wear track of the Al_2O_3/TiC substrate composites with grid texture after coating (Load=10N, sliding speed=20mm/s, time=30min). (a) Whole view of the wear track. (b) Enlarged area marked with a blue ellipse in the whole view

Plowing and cracks also could be found on the friction films of the wear track (Fig. 17 (b)). The friction films developed in the grid pattern (Fig. 17 (a)) are less substantial than those developed by the line pattern in (Fig. 15 (a)). It can be seen how in the coated grid case a smaller surface has suffered coating detachment compared to the coated line case. The smaller extension of the individual grid structures compared with the line ones, alongside the higher roughness, allow a more effective attachment of the coating which favours its survival to the wear test. At the same time, the continuous wearing of the coating

could also prompt the GNPs to be dragged out and form thin lubricant films, which to a certain extent counteracts the damage of the coating caused by the three-body abrasive wear from the higher amount of debris in the coated case which reduces the beneficial lubrication effect. The lower wear rates presented by the grid-textured samples after coating to those presented without coating could be attributed to the good capability of the grid grooves in capturing and displacing the wear debris, in addition to the pulling out of GNPs from the coating during the wear test to form thin lubricant films on the surface of the samples. It had been shown that fatigue spalling and abrasive wear were the main wear mechanisms for the alumina/GNPs coatings on the grid-textured samples.

3.7. Synergistic action of the alumina/GNPs coatings and the collection of wear particles in the grooves

As previously stated, a solid lubricant film of Ti_3O, Ti_6O and rutile TiO_2 as well as the reduction of contact area of the micro texture keeps the CoF of the sample with micro texture before coating at a relatively low value compared with those of Al_2O_3/TiC substrate composites without micro texture, which have been proved in some previous work [18, 60-61]. The wear track of the grid textured samples after coating showed the damage of the alumina/GNPs coating, which indicated that fatigue spalling and abrasive wear happened, generating a larger quantity of wear debris.

To elucidate the synergistic effect of the surface micro texture and the alumina/GNPs coating on the tribological performance of the Al_2O_3/TiC substrate composites, the schematic illustration of wear mechanism models for the tested specimens is presented in Fig. 18.
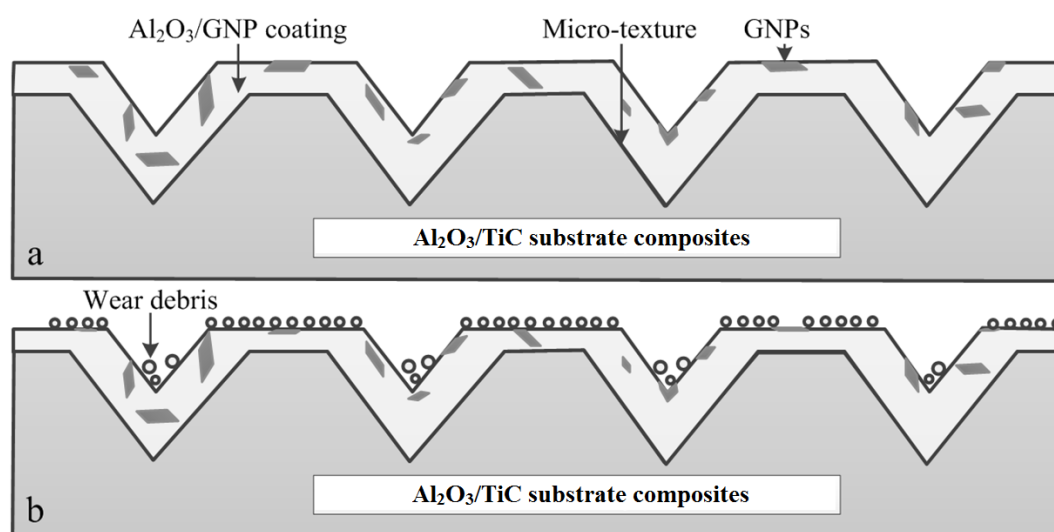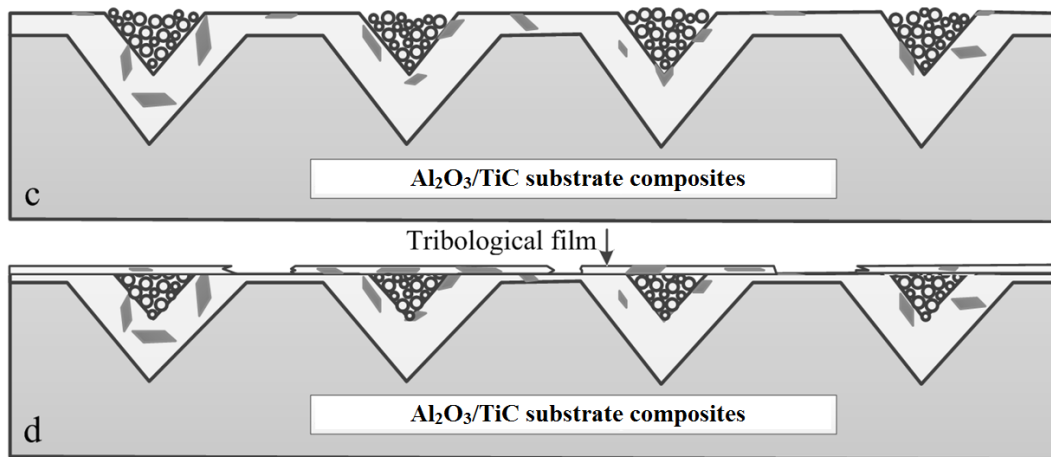
Fig. 18 schematic illustration of wear mechanism models for grid textured Al_2O_3/TiC substrate composites sprayed with alumina/GNPs coating. (a) GNPs were evenly dispersed in the alumina/GNPs coatings. (b) The alumina/GNPs coating was worn and debris is formed (c) As the wear test progressed, the debris tends to get trapped into the grooves resulting in complete filling and compacting, in particular along the wear track. (d) Throughout the process, GNPs were dragged out to form lubricant films, which could be favorable to reduce the friction of the contact surfaces

As depicted in Fig. 18 (a), before the sliding test, the alumina/GNPs coatings were deposited on the micro textured Al_2O_3/TiC substrate composites covering all the microtexture morphology, with GNPs evenly dispersed in the alumina matrix. Then, debris was formed during the in-opposite direction moving of the counterbody. Some of the debris spread out over the flat areas between the grooves, the remainder tended to get trapped into the grooves leading to complete filling and compacting, in particular along the wear track (Fig. 18 (b) and (c)). When the grooves were filled, some debris resulted in a very thin tribological film as well as the GNPs were dragged out to form lubricant films between the frictional pairs to act as a key role for decreasing the friction. With the ongoing experiment, micro cracks were firstly generated under high contact stress in the tribological films oriented at the flat areas between the grooves, and then fatigue spalling of the tribological films emerged (Fig. 18 (d)).

This process was repeated until the detachment of the last film appeared as was seen in Figs. 15 and 17. It should be noted that the tribological film at the top of the grooves might display a plastic deformation during the friction process, as a loose aggregates of the wear debris existed under the tribological film. And the tribological film at the flat areas between the grooves suffered from continuous pushing of the hard counterbody with high rigidity, which could explain why the micro cracks were firstly generated in the

tribological films oriented at the flat areas between the grooves and not at the top of the grooves. As in the case of the grid, the coating proved more wear resistance with the lower specific wear rate than the line (Fig.11). The grid texture has more grooves within a given area, thus linked to the above mechanism we could conclude that a high specific texture also contributed to the friction reduction.

As previously stated, micro cracks are generated under high contact stress, and finally fatigue spalling of the alumina/GNPs coating emerged and some coatings broke down forming wear debris during the sliding process (Fig. 18 (b)). The generated debris adheres to the surface might increase the adhesion between the sliding interfaces and then increase the CoF. However, some of the debris fell into the micro grooves and the surface micro texture served as entrapments of the wear debris reducing the abrasive wear. Furthermore, as the initial coating on the top layer of the wear track was worn off, GNPs were exposed and developed a thin self-lubricating film playing a significant role in the friction reduction. It could be concluded that the wear debris capturing capability of the micro grooves, as well as the dragging out of GNPs to create a thin self-lubricating film, leads to the better wear performance of the alumina/GNPs coated Al_2O_3/TiC substrate composites texturized with grid pattern.

4 Conclusions

A lubricating phase, GNPs, and a hard coating, alumina, together to improve the performance of Al_2O_3/TiC substrate composites with micro texture, fabricated by laser, was investigated in this paper. This is the first time to spray alumina/GNPs coatings on the micro textured top surfaces of Al_2O_3/TiC substrate composites using the SHVOF thermal spraying technique. The following conclusions were obtained:

1. Micro textures were fabricated on the top surface of the Al_2O_3/TiC substrate composites using the laser to generate a unique surface morphology. The original shape and structural characteristics of the micro texture still existed after coating, and the coatings had good spread ability and compaction.

2. Ti_3O and Ti_6O phases were formed during the texturing process. XRD analysis showed the formation of γ- Al_2O_3. The survival of the GNPs after spraying in the final coating, as well as after wear tests on the wear track, were confirmed by Raman spectroscopy.

3. The microhardness and fracture toughness of the alumina/GNPs coatings, by measuring the coating with a thickness of 30 µm, were (9.5 ± 2.0) GPa and (2.0 ± 0.7) MPa·m$^{1/2}$ respectively.

4. The alumina/GNPs coated Al_2O_3/TiC substrate composites textured with grid pattern showed the best tribological performance reaching a steady CoF at lower sliding distances and presenting the lowest wear

rate of the Al_2O_3/TiC substrate composites and the counterbody.

5. The main wear mechanisms of the alumina/GNPs coatings on the grid textured Al_2O_3/TiC substrate composites were fatigue spalling and abrasive wear, and that of on the line textured samples were brittle spalling, adhesive and abrasive wear.

6. The exposure of GNPs leads to the formation of self-lubricating GNPs films that contribute to the friction reduction of the investigated Al_2O_3/TiC substrate composites.

Acknowledgements

References

[1] Changxia Liu, Jianhua Zhang, Junlong Sun, Xihua Zhang, Tribological properties of pressureless sintered alumina matrix ceramic materials improved by diopside. Journal of the European Ceramic Society 28 (2008) 199-204. https://doi.org/10.1016/j.jeurceramsoc.2007.05.023.

[2] W. Grabon, W. Koszela, P. Pawlus, S. Ochwat. Improving tribological behavior of piston ring-cylinder liner frictional pair by liner surface texturing. Tribol. Int. 61(2013)102-108. https://doi.org/10.1016/j.triboint.2012.11.027.

[3] I. Etsion, E. Sher. Improving fuel efficiency with laser surface textured piston rings. Tribol. Int. 42(2009) 542-547. https://doi.org/10.1016/j.triboint.2008.02.015.

[4] N. P. Suh, M. Mosleh, P. S. Howard. Control of friction. Wear 175(1994)151–158.

[5] J. L. Li, D. S. Xiong, J. H. Dai, Z. J. Huang, R. Tyagi. Effect of surface laser texture on friction properties of nickel-based composite. Tribol Int. 43(2010)1193–1199. https://doi.org/10.1016/j.triboint.2009.12.044.

[6] X. L. Wang, K. Kato, K. Adachi, K. Aizawa. Load carrying capacity map for the surface texture design of SiC thrust bearing sliding in water. Tribol Int. 36 (2003) 189–197. https://doi.org/10.1016/S0301-679X(02)00145-7.

[7] C. Sinanoglu. Investigation of load carriage capacity of journal bearings by surface texturing. Ind Lubr Tribol. 61(2009)261–270.

[8] N. Tala-lghil, M. Fillon, P. Maspeyrot. Effect of textured area on the performances of a hydrodynamic journal bearing. Tribol Int. 44(2011)211–219. https://doi.org/10.1016/j.triboint.2010.10.003.

[9] P. Pawlus, L. Galda, A. Dzierwa, W. Koszela. Abrasive wear resistance of textured steel rings. Wear. 267(2009)1873–1882. https://doi.org/10.1016/j.wear.2009.03.003.

[10] I. Etsion, E. Sher. Improving fuel efficiency with laser surface textured piston rings. Tribol Int.

42(2009)542–547. https://doi.org/10.1016/j.triboint.2008.02.015.

[11] T. Enomoto, T. Sugihara. Improving anti-adhesive properties of cutting tool surfaces by nano-/micro-textures. CIRP Annals-Manufacturing Technology 59(1) (2010)597-600. https://doi.org/10.1016/ j.cirp.2010.03.130.

[12] T. Enomoto and T. Sugihara. Improvement of anti-adhesive properties of cutting tool by nano/micro textures and its mechanism. Procedia Engineering 19(1) (2011) 100-105. https://doi.org/10.1016/j.proeng.2011.11.086.

[13] T. Enomoto, T. Sugihara, S. Yukinaga. Highly wear-resistant cutting tools with textured surfaces in steel cutting. CIRP Annals-Manufacturing Technology 61(1) (2012) 571–574. https://doi.org/10.1016/j.cirp.2012.03. 123.

[14] Toshiyuki Obikawa, Akihiro Kamio, Hidemitsu Takaoka, Akira Osada. Micro-texture at the coated tool face for high performance cutting. International Journal of Machine Tools and Manufacture 51(12) (2011) 966-972. https://doi.org/10.1016/j.ijmachtools.2011.08.013.

[15] Jianxin Deng, Yunsong Lian, Ze Wu, Youqiang Xing. Performance of femtosecond laser-textured cutting tools deposited with WS_2 solid lubricant coatings. Surface and Coatings Technology 222(1) (2013)135-143. https://doi.org/10.1016/j.surfcoat.2013.02.015.

[16] Kedong Zhang, Jianxin Deng, Zeliang Ding, Xuhong Guo, Lining Sun. Improving dry machining performance of TiAlN hard-coated tools through combined technology of femtosecond laser-textures and WS_2 soft-coatings. Journal of Manufacturing Processes 30 (2017) 492-501. https://doi.org/10.1016/j.jmapro.2017.10.018.

[17] Rong Meng, Jianxin Deng, Yayun Liu, Ran Duan, Guiliang Zhang. Improving tribological performance of cemented carbides by combining laser surface texturing and W-S-C solid lubricant coating. International Journal of Refractory Metals and Hard Materials 72 (2018) 163-171. https://doi.org/10.1016/j.ijrmhm.2017.12.024.

[18] Xuemu Li, Jianxin Deng, Liangliang Zhang, Yayun Liu, Hongzhi Yue, Ran Duan, Dongliang Ge. Effect of surface textures and electrohydrodynamically atomized WS_2 films on the friction and wear properties of ZrO_2 coatings. Ceramics International 45(1) (2019) 1020-1030. https://doi.org/10.1016/j.ceramint.2018.09.281.

[19] A. Gallardo-López, I. Márquez-Abril, A. Morales-Rodríguez, A. Muñoz, R. Poyato. Dense graphene nanoplatelet/yttria tetragonal zirconia composites: Processing, hardness and electrical conductivity. Ceramics International 43 (2017) 11743–11752. https://doi.org/10.1016/j.ceramint.2017.06.007.

[20] Y. Liu, Z. Dang, Y. Wang, J. Huang, H. Li. Hydroxyapatite/graphene-nanosheet composite coatings deposited by vacuum cold spraying for biomedical applications: inherited nanostructures and enhanced properties. Carbon 67(1) (2014) 250–259. https://doi.org/10.1016/j.carbon.2013.09.088.

[21] C. Ramirez, M.I. Osendi. Toughening in ceramics containing graphene fillers. Ceramics International 40 (7) (2014) 11187–11192. https://doi.org/10.1016/j.ceramint.2014.03.150.

[22] T. Thomas, C. Zhang, A. Sahu, P. Nautiyal, A. Loganathan, T. Laha, B. Boesl, A. Agarwal. Effect of graphene reinforcement on the mechanical properties of Ti_2AlC ceramic fabricated by spark plasma sintering. Materials Science & Engineering A 728 (2018) 45–53. https://doi.org/10.1016/j.msea.2018.05.006.

[23] G.B. Yadhukulakrishnan, S. Karumuri, A. Rahman, R.P. Singh, A.K. Kalkan, S.P. Harimkar. Spark plasma sintering of graphene reinforced zirconium diboride ultra-high temperature ceramic composites. Ceramics International 39 (6) (2013) 6637–6646. https://doi.org/10.1016/j.ceramint.2013.01.101.

[24] H. Porwal, R. Saggar, P. Tatarko, S. Grasso, T. Saunders, I. Dlouhý, M. J. Reece. Effect of lateral size of graphene nano-sheets on the mechanical properties and machinability of alumina nano-composites. Ceramics International 42 (2016) 7533–7542. https://doi.org/10.1016/j.ceramint.2016.01.160.

[25] M. Belmonte, C. Ramirez, J. Gonzalez-Julian, J. Schneider, P. Miranzo, M.I. Osendi. The beneficial effect of graphene nanofillers on the tribological performance of ceramics. Carbon 61 (1) (2013) 431–435. https://doi.org/10.1016/j.carbon.2013.04.102.

[26] ZengbinYin, JuntangYuan, Weiwei Xu, Mingdan Chen, Shiyu Yan, Zhenhua Wang. Effect of Ni and graphene on microstructure and toughness of titanium boride ceramic tool material prepared by spark plasma sintering. Ceramics International 44 (2018) 20299-20305. https://doi.org/10.1016/j.ceramint.2018.08.017.

[27] J.W. Murray, G.A. Rance, F. Xu, T. Hussain. Alumina-graphene nanocomposite coatings fabricated by suspension high velocity oxy-fuel thermal spraying for ultra-low-wear. Journal of the European Ceramic Society 38 (2018) 1819–1828. https://doi.org/10.1016/j.jeurceramsoc.2017.10.022.

[28] Yehong Cheng, Ping Hu, Shanbao Zhou, Xinghong Zhang, Wenbo Han. Using macroporous graphene networks to toughen ZrC–SiC ceramic. Journal of the European Ceramic Society 38(2018) 3752-3758. https://doi.org/10.1016/j.jeurceramsoc.2018.04.037.

[29] Xuchao Wang, Jun Zhao, Enzhao Cui, Hao Liu, Youhao Dong, Zhefei Sun. Effects of sintering parameters on microstructure, graphene structure stability and mechanical properties of graphene reinforced Al_2O_3-based composite ceramic tool material. Ceramics International 45 (2019) 23384-23392. https://doi.org/10.1016/j.ceramint.2019.08.040.

[30] F. Gutiérrez-Mora, A. Morales-Rodríguez, A. Gallardo-López, R. Poyato. Tribological behavior of graphene nanoplatelet reinforced 3YTZP composites. Journal of the European Ceramic Society 39 (2019) 1381–1388. https://doi.org/10.1016/j.jeurceramsoc.2018.11.005.

[31] Jingbao Zhang, Jingjie Zhang, Guangchun Xiao, Zhaoqiang Chen, Mingdong Yi, Yubing Zhang, Chonghai Xu. Orentational effect of graphene on the friction and wear behavior of Si3N4/ TiC based composite ceramic tool materials. Ceramics International 46 (2020) 3550-3557. https://doi.org/10.1016/j.ceramint.2019.10.072.

[32] A.G. Evans, E.A. Charles. Fracture toughness determination by indentation. J. Am. Ceram. Soc. 59 (1976) 371–372.

[33] W.L. Ma, J.J. Lu. Effect of surface texture on transfer layer formation and tribological behavior of copper–graphite composite. Wear 270 (2011) 218–229. https://doi.org/10.1016/j.wear.2010.10.062.

[34] C.X. He. Advanced Mathematics, Tsinghua University Press, Beijing, 2009.

[35] F.J.C. Braga, R.F.C. Marques, E. de A. Filho, A.C. Guastaldi. Surface modification of Ti dental implants by Nd:YVO_4 laser irradiation. Applied Surface Science 253 (2007) 9203–9208. https://doi.org/10.1016/j.apsusc.2007.05.048.

[36] A. Pérez del Pino, P. Serra, J.L. Morenza. Coloring of titanium by pulsed laser processing in air. Thin Solid Films 415 (2002) 201–205. https://doi.org/10.1016/S0040-6090(02)00632-6.

[37] L. Na´nai, R. Vajtai, T.F. George. Laser-induced oxidation of metals: state of the art. Thin Solid Films 298 (1997) 160–164. https://doi.org/10.1016/S0040-6090(96)09390-X.

[38] L. Lavisse, D. Grevey, C. Langlade, B. Vannes. The early stage of the laser-induced oxidation of titanium substrates. Appl. Surf. Sci. 186 (2002) 150–155. https://doi.org/10.1016/S0169-4332(01)00761-9.

[39] Y. Xing, L. Liu, Z. Wu, X. Wang, P. Huang, L. Tang. Fabrication and characterization of micro-channel on Al_2O_3/TiC ceramic produced by nanosecond laser. Ceramics International 44 (2018) 23035–23044. https://doi.org/10.1016/j.ceramint.2018.09.106.

[40] R. Shi, J. Ding, Y. Cao, A. Zhang, P. Yang. Oxidation behavior and kinetics of Al_2O_3–TiC–Co composites. Int. Journal of Refractory Metals and Hard Materials 36 (2013) 130–135. https://doi.org/10.1016/j.ijrmhm.2012.08.005.

[41] F. Rejasse, G. Trolliard, J. Lechelle, O. Rapaud, P. Carles, O. Grauby, H. Khodja. Study of the TiC_{1-x}- TiO_2 reactive interface. Acta Materialia 146 (2018) 225-236. https://doi.org/10.1016/j.actamat.2017.12.055.

[42] S. Yoshioka, L. Boatemaa, S. van der Zwaag, W. Nakao, W. G. Sloof. On the use of TiC as high-temperature healing particles in alumina based composites. Journal of the European Ceramic Society 36 (2016) 4155–4162. https://doi.org/10.1016/j.jeurceramsoc.2016.06.008.

[43] R.X. Shi, K. Li, A.Y. Zhang, Y.Q. Cao, P. Yang. Oxidation behaviour of Al_2O_3–TiC–Co composites at 800–1000 °C in air. Corros Sci 53 (2011) 4058-4064. https://doi.org/10.1016/j.corsci.2011.08.008.

[44] Q.L. Wu, J.Q. Zhang, Y.S. Sun. Oxidation behaviour of TiC particle-reinforced 304 stainless steel. Corros Sci 52 (2010) 1003-1010. https://doi.org/10.1016/j.corsci.2009.11.025.

[45] Z.F. Yang, W.J. Lu, J.N. Qin, D. Zhang. Oxidation behaviour of in situ synthesized (TiC+TiB+Nd2O3)/Ti composites. Mater Sci Eng A 472 (2008) 187-192. https://doi.org/10.1016/j.msea.2007.03.058.

[46] Y.X. Qin, W.J. Lu, D. Zhang, J.N. Qin, B. Ji. Oxidation of in situ synthesized TiC particle-reinforced titanium matrix composites. Mater Sci Eng A 404 (2005) 42-48. https://doi.org/10.1016/j.msea.2005.05.098.

[47] T.A.Owoseni, J.W.Murray, Z.Pala, E.H.Lester, D.M.Grant, T.Hussain. Suspension high velocity oxy-fuel (SHVOF) spray of delta-theta alumina suspension: Phase transformation and tribology. Surface and Coatings Technology 371(2019) 97-106. https://doi.org/10.1016/j.surfcoat.2018.08.047.

[48] B. Yazdani, F. Xu, I. Ahmad, X. Hou, Y. Xia, Y. Zhu. Tribological performance of Graphene/Carbon nanotube hybrid reinforced Al_2O_3 composites. Sci. Rep. 5 (2015) 11579. https://doi.org/10.1038/srep11579

[49] H. Xu, X. Wu, X. Li, C. Luo, F. Liang, E. Orignac, J. Zhang, J. Chu. Properties of graphene-metal contacts probed by Raman spectroscopy. Carbon 127 (2018) 491-497. https://doi.org/10.1016/j.carbon.2017.11.035.

[50] Mildred.S. Dresselhaus, Ado Jorio, Mario Hofmann, Gene Dresselhaus, Riichiro Saito. Perspectives on carbon nanotubes and graphene raman spectroscopy. Nano Lett. 10 (3) (2010) 751–758. https://doi.org/10.1021/nl904286r

[51] F. Venturi, G. A. Rance, J. Thomas, and T. Hussain. A low-friction graphene nanoplatelets film from suspension high velocity oxy-fuel thermal spray. AIP Advances 9, 025216 (2019) https://doi.org/10.1063/1.5089021

[52] Y. Xing, J. Deng, X. Wang, R. Meng. Effect of laser surface textures combined with muli-solid lubricant coatings on the tribolobical properties of Al_2O_3/TiC ceramic. Wear 342-343 (2015) 1-12. https://doi.org/10.1016/j.wear.2015.08.002.

[53] M.K.A. Ali, H. Xianjun, L. Mai, C. Qingping, R.F. Turkson, C. Bicheng. Improving the tribological characteristics of piston ring assembly in automotive engines using Al_2O_3 and TiO_2 nanomaterials as nano-lubricant additives. Tribology International 103 (2016) 540-554. https://doi.org/10.1016/j.triboint.2016.08.011.

[54] R.K. Sabareesh, N. Gobinath, V. Sajith, Sumitesh Das, C. B. Sobhan. Application of TiO_2 nanoparticles as a lubricant-additive for vapor compression refrigeration systems – An experimental investigation. International Journal of Refrigeration. 35(7) (2012) 1989-1996. https://doi.org/10.1016/j.ijrefrig.2012.07.002.

[55] G. Jatinder, O.S. Ohunakin, D.S. Adelekan, O.E. Atiba, A.B. Daniel, J. Singh, A. A. Atayero. Performance of a domestic refrigerator using selected hydrocarbon working fluids and TiO_2–MO nanolubricant. Applied Thermal Engineering, 160 (2019) No. 114004. https://doi.org/10.1016/j.applthermaleng.2019.114004.

[56] T. Luo, X. Wei, H. Zhao, G. Cai, X. Zheng. Tribology properties of Al_2O_3/TiO_2 nanocomposites as lubricant additives. Ceramics International 40(7) Part A (2014) 10103-10109. https://doi.org/10.1016/j.ceramint.2014.03.181.

[57] I. Lukačević, S. K. Gupta, P. K. Jha, D. Kirin. Lattice dynamics and Raman spectrum of rutile TiO_2: the role of soft phonon modes in pressure induced phase transition. Mater Chem Phys 137(2012)282-289. https://doi.org/10.1016/j.matchemphys.2012.09.022.

[58] C. Magnus, T. Kwamman, W.M. Rainforth. Dry sliding friction and wear behaviour of TiC-based ceramics and consequent effect of the evolution of grain buckling on wear mechanism. Wear 422-423 (2019) 54-67. https://doi.org/10.1016/j.wear.2019.01.026.

[59] Bowen Zheng, Fuyu Dong, Xiaoguang Yuan, Hongjun Huang, Yue Zhang, Xiaojiao Zuo, Liangshun Luo, Liang Wang, Yanqing Su, Weidong Li, Peter K. Liaw, Xuan Wang. Microstructure and tribological behavior of in situ synthesized (TiB+TiC)/Ti6Al4V (TiB/TiC=1/1) composites. Tribology International 145 (2020) 106177. https://doi.org/10.1016/j.triboint.2020.106177.

[60] Y.Q. Xing, J.X. Deng, Y.H. Zhou, S.P. Li. Fabrication and tribological properties of Al_2O_3/TiC ceramic with nano-textures and WS_2/Zr soft coatings. Surf. Coat. Technol. 258 (2014) 699-710. https://doi.org/10.1016/j.surfcoat.2014.08.014.

[61] X. Li, J. Deng, L. Liu, L. Zhang, J. Sun, D. Ge, Y. Liu, R. Duan. Tribological properties of WS2 coating deposited on textured surfaces by electrohydrodynamic atomization. Surface & Coatings Technology 352 (2018) 128-143. https://doi.org/10.1016/j.surfcoat.2018.08.011.